Numerical Study of Static and Vortex-Induced Vibrations of Normal and Yawed Cylinder with Detached Eddy Simulations

Xingeng Wu[1], Mohammad Jafari[1], Partha Sarkar[2], Anupam Sharma[3,*]

Department of Aerospace Engineering, Iowa State University, Ames, Iowa, 50011

Abstract

A computational approach based on a $k - \omega$ delayed detached eddy simulation (DDES) model for predicting aerodynamic loads on a smooth circular cylinder is verified against experiments. Comparisons with data are performed for a stationary cylinder and for a cylinder oscillating in the transverse direction due to flow-induced forces (vortex induced vibration or VIV). For the static cases, measurement data from the literature is used to validate the predictions for normally-incident flow. New experiments are conducted as a part of this study for yawed flow, where the cylinder axis is inclined with respect to the inflow velocity at the desired yaw angle, $\beta = 30°$. Good agreement is observed between the predictions and measurements for mean and rms surface pressure and wake velocity deficit. However the lift spectrum prediction shows a slight offset in frequency from the measurements. Three yawed flow cases ($\beta = 15°, 30°, \& 45°$) are simulated and the results are found to be independent of β (dynamic scaling) when the flow speed normal to the cylinder axis is selected as the reference velocity scale.

The VIV simulations are performed by coupling the flow solver with a solid dynamics solver where the cylinder motion in the transverse direction is modeled as a spring-mass-damper system. The properties of the spring, mass, and damper are set to match the material

---

*Corresponding author
  Email address:* `sharma@iastate.edu` (Anupam Sharma)
[1]Graduate Student
[2]Professor, Iowa State University
[3]Associate Professor, Iowa State University

properties of the cylinder model used in a VIV experiment available in the literature.

The numerical study for the normal flow of vortex-induced vibration (VIV) for various reduced velocities shows reasonable agreement with experiments. The predicted mean amplitude and force coefficients for normal flow and yawed flow ($\beta = 45°$) in VIV simulations are very similar in most regime except for the upper branch.

1. Introduction

Inclined and horizontally- or vertically-spanned cylinder are used in various engineering applications: cable-stayed, suspension, and tied-arch bridges, power transmission lines, offshore risers, sub-sea pipelines etc. These cylinders are prone to large-amplitude flow-induced vibration, which can lead to catastrophic failure of the cylinders and the structures supported by them. The vibration mechanisms involve complex aeroelastic (motion-induced) interactions that depend on the spatial orientation, geometry, surface-characteristics, and dynamic properties of cylinders. Davenport (1995) shows that large amplitude vibrations can lead to either catastrophic- or fatigue failure of the cylinders and/or the adjoining structures, which poses a significant threat to the safety and serviceability of these systems.

Vortex-induced vibration(VIV) is an oscillating motion due to the interaction between structures and periodical vortexes. VIV is a very common vibration phenomenon happened in many engineering areas, such as offshore structures, transmission lines, stacks, and bridges. Due to its practical significance in many engineering structures, VIV has raised many interests and been extensively investigated in past decades. Bearman (1984), Sarpkaya (2004) and Williamson and Govardhan (2004) have done some detailed reviews of the these work. One of the most important observations of VIV is called "lock-in" or "synchronization". "Lock-in" is a regime where shedding vortexes induce large response amplitude of the struc-

tures because the oscillating frequency along with vortex shedding frequency lock onto the natural frequency of the structures. Feng (1968) observed two amplitude branches in the "lock-in" regime in experiment. Because this experiment was carried in wind tunnels, the system has a very large mass ratio. The jump between two branches was suspected due to the change of vortex shedding mode. However, in recent years, other different amplitude branches have been found in water tunnel tests which have much small mass ratio. Four branches have been identified and labeled as "initial excitation", "upper branch", "lower branch" and "desynchronization".(Khalak and Williamson (1997)).

Past investigations of VIV were based primarily on experiments and a limited number of computational fluid dynamics (CFD). These studies, spanning over the past several decades, have resulted in an improved understanding of the phenomenon of the VIV, particularly when the flow is perpendicular to the cylinder in wind tunnel. However, most of these work investigated relatively large mass and damping system. In recent years, due to increasing applications of marine engineering, VIV of low mass and damping system has raised many interests and been widely studied in experiments. Though a lot of experimental studies have been done in this decade, only a very few studies were related to the VIV of a yawed cylinder with low mass and damping. These experiments (Jain and Modarres-Sadeghi (2013), Franzini et al. (2013)) were performed to validate the independence principle on the oscillating frequency, amplitude and force coefficients of an elastically-mounted cylinder with various yawed angles. The experiments are conducted in water tunnels with a partially submerged yawed cylinder. Due to the effects of the end conditions, these experiments observed different results between the cylinder slanted towards upstream and downstream. Ideally, the independence principle should be investigated without any end effect because the vortex shedding of a yawed stationary cylinder and the response of an elastically-mounted cylinder are both very sensitive to the end conditions. Compared with experiments, simulations are much easier to achieve the end-effect-free result. Zhao (2015) studied the independence prin-

ciple of an elastically-mounted cylinder for two Reynolds numbers (Re=150 and Re=1,000) by using direct numerical simulation (DNS) and periodic boundary conditions. Independence principle for the response amplitude and frequency is observed on this numerical study, but the Reynolds numbers of this study are very small.

This paper presents the results of our progress towards the goal of developing an aeroelastic load model for cylinder vibration. The objective is to be able to accurately predict aerodynamic loading on a single, smooth circular cylinder operating in smooth inflow (normal and yawed flow) for static and dynamic conditions. This paper focuses on verifying the computational methodology against experimental data for normally-incident flow and yawed flow.

2. Computational Methodology

The flow is approximated to be incompressible since the flow Mach number is less than 0.2. Various degrees of approximations can be utilized to model flow turbulence: from resolving only time-averaged quantities in Reynolds Averaged Navier-Stokes or RANS, to resolving the tiniest of turbulent eddies in Direct Numerical Simulations or DNS. Large eddy simulations (LES) resolve energy containing eddies but model the net effect of smaller (unresolved/universal) eddies on larger (resolved) eddies. The detached eddy simulation (DES) technique (Spalart et al., 1997) is a hybrid approach that uses RANS equations to simulate attached flow near solid surfaces and LES for separated (detached) flow away from the surfaces. DES allows computation of high Reynolds number flows relatively inexpensively by removing the constraint in LES to have very fine grids near solid boundaries.

Flow over slender structures with circular cross-section has been studied using unsteady RANS (Pontaza et al., 2009), DES (Travin et al., 2000; Yeo and Jones, 2012), LES (Breuer, 1998; Kravchenko and Moin, 2000; Catalano et al., 2003), and DNS (Dong and Karniadakis, 2005; Zhao et al., 2009) approaches. Latest numerical efforts in simulating aerodynamics

4

of cable vibration have utilized DES (Yeo et al., 2007; Yeo and Jones, 2008, 2012, 2011) as the primary numerical approach. Detailed flow simulations have been performed with a single, stationary, yawed cylinder in uniform inflow (Yeo et al., 2007; Yeo and Jones, 2008) and oscillating inflow (Yeo and Jones, 2012). It has been concluded by Yeo and Jones (2012) that oblique wind-induced aerodynamic forces play an important role in initiating and increasing the vibration at low frequencies. DES has also been used to investigate the use of strakes in cables for aerodynamic mitigation of wind-induced oscillations by Yeo and Jones (2011). In essence, high-fidelity simulations have been instrumental in gaining insights into the problem of flow-induced cylinder vibration.

In LES and DES, the equations are spatially filtered (low-pass) and the numerical procedure solves for the filtered quantities that can be resolved by the grid. The sub-filter (or sub-grid) quantities exert a "stress" on the filtered flow-field, which is modeled using a sub-grid scale (SGS) stress model. Denoting spatially filtered quantities by overhead tilde (~), the incompressible flow equations with an eddy-viscosity turbulence model are

$$\frac{\partial \tilde{U}_i}{\partial x_i} = 0, \text{ and}$$

$$\frac{\partial \tilde{U}_i}{\partial t} + \frac{\partial (\tilde{U}_j \tilde{U}_i)}{\partial x_j} = -\frac{1}{\rho}\frac{\partial \tilde{p}}{\partial x_i} + \nu \frac{\partial^2 \tilde{U}_i}{\partial x_j^2} - \frac{\partial \tau_{ij}}{\partial x_j},$$

where $\tau_{ij} = \widetilde{U_i U_j} - \tilde{U}_i \tilde{U}_j = -2\,\nu_{SGS}\,\tilde{S}$ and $\tilde{S} = (\partial \tilde{U}_i/\partial x_j + \partial \tilde{U}_j/\partial x_i)/2$. In the above, SGS denotes a sub-grid scale quantity, τ_{ij}^{SGS} denotes the sub-grid scale stress tensor which is modeled as the product of eddy viscosity, ν_{SGS} and the strain rate tensor S_{ij}; turbulence models of such type are referred to as eddy-viscosity models. DES is a non-zonal hybrid RANS-LES method, where a RANS turbulence model is used to compute the eddy viscosity for the SGS stress tensor in the corresponding LES. In the original DES formulation (Spalart et al. (1997)), the Spalart-Allmaras (SA) LES and SA-RANS models were used. We use the method developed by Yin et al. (2015), which introduces a dynamic procedure to improve

5

the DES capability by correcting for modeled stress depletion and log-layer mismatch. This model has been implemented in the open source CFD software OpenFOAM. All the simulations in this paper are obtained using OpenFOAM. The numerical scheme uses second order backward difference for time integration and linear interpolation with central differencing for spatial discretization of the governing equations.

Simulations of VIV are using pimpleDyMFoam solver with sixDoFRigidBodyMotion feature on OpenFOAM. The incompressible Navier-Stokes equations are solved by pimpleDyM-Foam solver. For VIV cases, the incompressible Navier-Stokes equations includes an addition body force term due to interaction between the moving cylinder and fluid.

$$m\ddot{Y} + c\dot{Y} + kY = F_{fluid},$$

where m is the mass of the rigid body, $\ddot{Y}$, $\dot{Y}$, and Y are the instantaneous acceleration, velocity and displacement of the cylinder, respectively, c is spring damping, k is the spring stiffness and F_{fluid} is the fluid forces applying on the cylinder solved by Navier-Stokes equations.

2.1. Detached Eddy Simulation Model

A summary of the DES model used in this study is provided here; details are available in Yin et al. (2015). It uses a $k - \omega$ turbulence closure model in the RANS zones, and the same model is used to calculate ν_T in the LES zones. The eddy viscosity in the $k - \omega$ DDES can be defined as $\nu_T = l_{DDES}^2 \omega$, where l_{DDES} is the DDES length scale. The different length scales in the $k - \omega$ DDES model are defined as

$$l_{DDES} = l_{RANS} - f_d \max(0, \ l_{RANS} - l_{LES}),$$

$$l_{RANS} = \sqrt{k}/\omega,$$

$$l_{LES} = C_{DES} \triangle .$$

In the above, l_{RANS} and l_{LES} are the length scales of the RANS and LES branches respectively and $\triangle = f_d V^{1/3} + (1 - f_d) h_{max}$, where $h_{max} = \max(dx, dy, dz)$ is the maximum grid

6

size, and f_d is a shielding function of the DDES model, defined as $f_d = 1 - \tanh\{(8\,r_d)^3\}$, with

$$r_d = \frac{k/\omega + \nu}{\kappa^2\,d_w^2\,\sqrt{U_{i,j}U_{i,j}}},$$

ν is the molecular viscosity, κ is the von Karman constant, d_w is the distance between the cell and the nearest wall, and $U_{i,j} = \partial_j U_i$ is the velocity gradient. In the RANS branch, the transport equation for k and ω are written as

$$\frac{Dk}{Dt} = 2\nu_T |S|^2 - C_\mu k\omega + \partial_j[(\nu + \sigma_k \nu_T)\partial_j k],$$
$$\frac{D\omega}{Dt} = 2C_{\omega 1}|S|^2 - C_{\omega 2}\omega^2 + \partial_j[(\nu + \sigma_\omega \nu_T)\partial_j \omega],$$

$$\text{where } \nu_\mathrm{T} = \mathrm{k}^2/\omega.$$

In the LES region ($f_d = 1$, $l_{DDES} = C_{DES}\,\triangle$), the eddy viscosity switches to $\nu_T = l^2_{DDES}\,\omega = (C_{DES}\triangle)^2\omega$, which is similar to the eddy viscosity in the Smagorinsky model, $\nu_s = (C_s\triangle)^2|S|$.

The LES branch of this $k - \omega$ DDES model uses a dynamic procedure which defines the value of C_{DES} as

$$C_{DES} = \max(C_{lm},\ C_{dyn}),$$
$$C^2_{dyn} = \max\left(0,\ 0.5\frac{L_{i,j}M_{i,j}}{M_{i,j}M_{i,j}}\right),$$
$$C_{lim} = C^0_{DES}\left[1 - \tanh\left(\alpha\exp\left(\frac{-\beta\,h_{max}}{L_k}\right)\right)\right],$$
$$C^0_{DES} = 0.12,\quad L_k = \left(\frac{\nu^3}{\epsilon}\right)^{\frac{1}{4}},\quad \alpha = 25,\quad \beta = 0.05,$$
$$\epsilon = 2\left(C^0_{DES}h_{max}\right)^2 \omega\,|S|^2 + C_\mu k\,\omega.$$

For further details about the DES model, the reader is referred to Yin et al. (2015).

2.2. Computational Grids

The outer boundary of the computational domain is circular with a radius of $25 \times D$, where D is the diameter of the cylinder. The cylinder is placed in the center of the domain

and the span dimension is $10 \times D$ for all simulations. Periodic boundary conditions are used in the span direction, while freestream condition is used on the outer radial boundary. The domain is discretized using a multi-block grid that has three blocks: (1) an O-grid is used to resolve the flow around the cylinder, (2) an H-grid to resolve the wake, and (3) a C-grid for the far field. In order to accurately capture the aerodynamic forces on the cylinder, the flow around the cylinder and in the near-wake region has to be resolved with high precision. A fine mesh is therefore applied in these regions. Figure 1 shows a cross-sectional view of the full computational domain as well as a zoom-view to highlight the grid topology. Results of a mesh sensitivity study are presented in Section 4.1.


(a) Overall CFD domain

(b) Zoom view of near-cylinder mesh
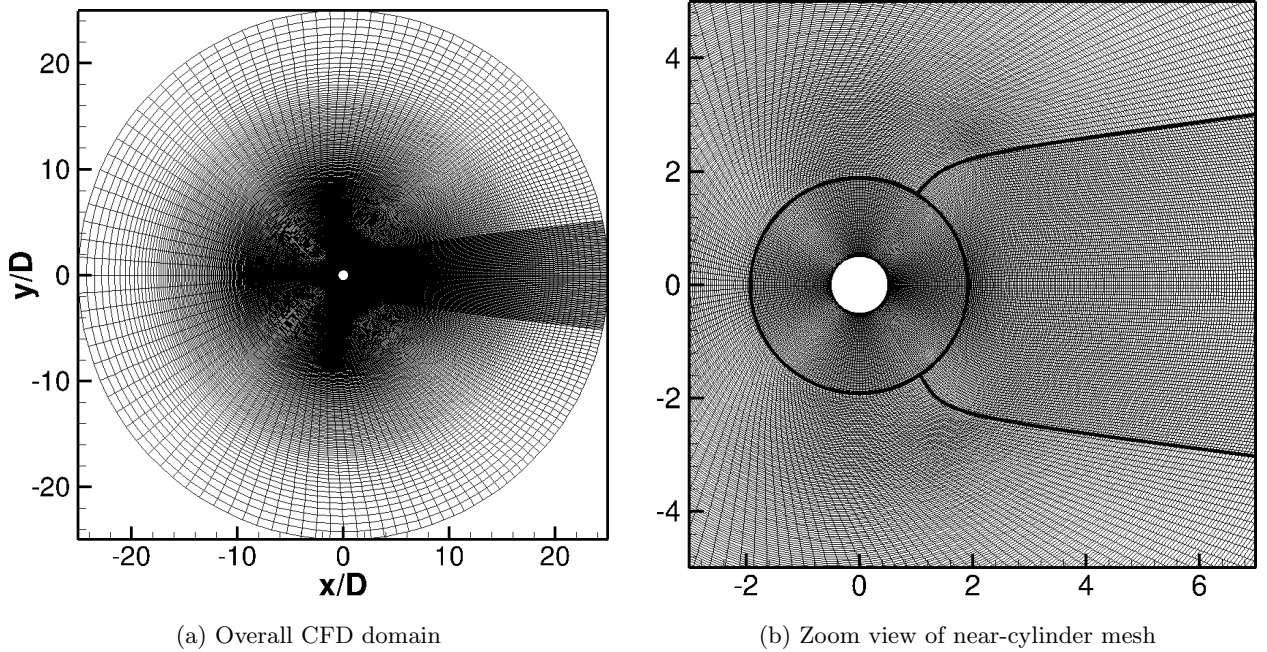
Figure 1: Cross-sectional views of the computational grid

3. Experimental Setup and Measurements

Static wind tunnel experiments were conducted on a smooth cylinder of circular cross section representing a stay cable to measure the aerodynamic forces and the velocity distribution in its wake. These experiments were performed in the Aerodynamic/Atmospheric

8

Boundary Layer (AABL) Wind and Gust Tunnel located in the Department of Aerospace Engineering at Iowa State University. This wind tunnel has an aerodynamic test section of 2.44 m (8.0 ft) width $\times$ 1.83 m (6.0 ft) height and a design maximum wind speed of 53 m/s (173.9 ft/s). A polished aluminum tube with diameter, $D = 0.127$ m and length, $L = 1.52$ m was selected as the smooth cylinder model. Although the aspect ratio ($L/D = 12$) is sufficiently large to minimize edge effects at the mid-span of the circular cylinder, two circular plates of diameter $4\,D$ were attached to the ends of the cylinder. These plates were adjusted for each cylinder yaw angle to be parallel to the incoming airflow so that nearly 2D flow could be achieved over the cylinder. The blockage ratio in the tunnel with the model was approximately 5% for all measurements. Figure 2 displays the model setup in the AABL tunnel with the cylinder in normal-flow and yawed-flow configurations. An innovative multi-functional static setup was designed to measure the pressure distributions and velocity profiles for different yaw angles. As shown in Fig. 2, this setup properly secures the model for different yaw angles.
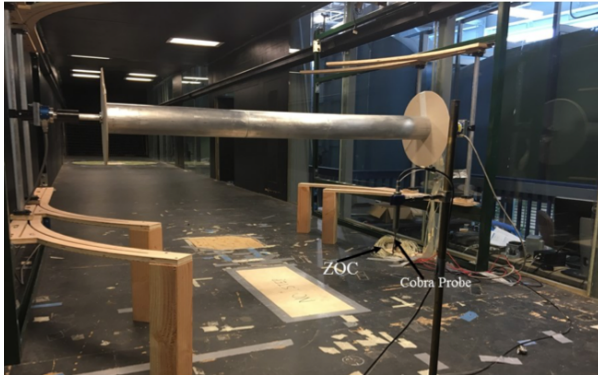
(a) setup for normal-flow measurements
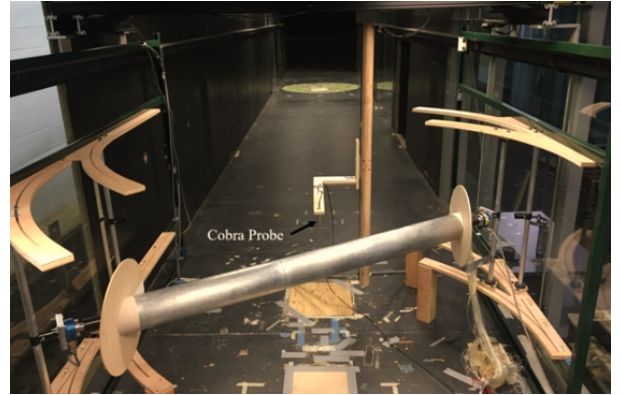
(b) setup for yawed flow measurements

Figure 2: Pictures showing the model setup used to allow measurements at arbitrary inflow angles. The Cobra probe used to measure the wake is shown in (a).

The model has 128 pressure taps distributed on its surface to measure local instantaneous pressure (see Fig. 3). These pressure values are used to compute aerodynamic lift and drag

(viscous part ignored) on the cylinder as well as pressure correlations along the span. There are 36 pressure taps at equal angular spacing of 10 degrees along each of the three rings located on the cylinder. The three rings are labeled Right (R), Middle (M), and Left (L) as seen in Fig. 3 (a) and are spaced $4D$ and $5D$ apart from each other along the span. Another set of pressure taps are located at a fixed angular location at equal spacing of $1D$ along the span between the rings (see Fig. 3 (a,b)).

3.1. Data Acquisition System

For wake measurement, one Cobra Probe (4-hole velocity probe) mounted on a traverse system was used to measure the velocity field behind the model (see Fig. 2 (a)). In order to minimize the blockage effect of the traverse system, its cross section was streamlined by using an airfoil section. For velocity measurements, the sampling rate was 1250 Hz and the sampling time was 60 s. Wake measurements were made $2.5D$ downstream of the model (measured from the cylinder axis), where the turbulence intensity was lower than the maximum allowable value (overall 30%) for the Cobra Probe.

Two 64-channel pressure modules (Scanivalve ZOC 33/64 Px) were utilized to capture the local pressure. In addition, an Ethernet remote A/D system (ERAD) was used as a collection system to read information from the ZOC. The sampling rate and sampling time for all pressure measurements were 250 Hz and 60 s respectively. The Scantel program from Scanivalve was used for pressure data acquisition. In order to minimize the error of measurement due to the tube length, both ZOCs were placed inside the wind tunnel near the model (Fig. 2 (b)). The wake measurement traverse system was removed when surface pressure measurements were made.
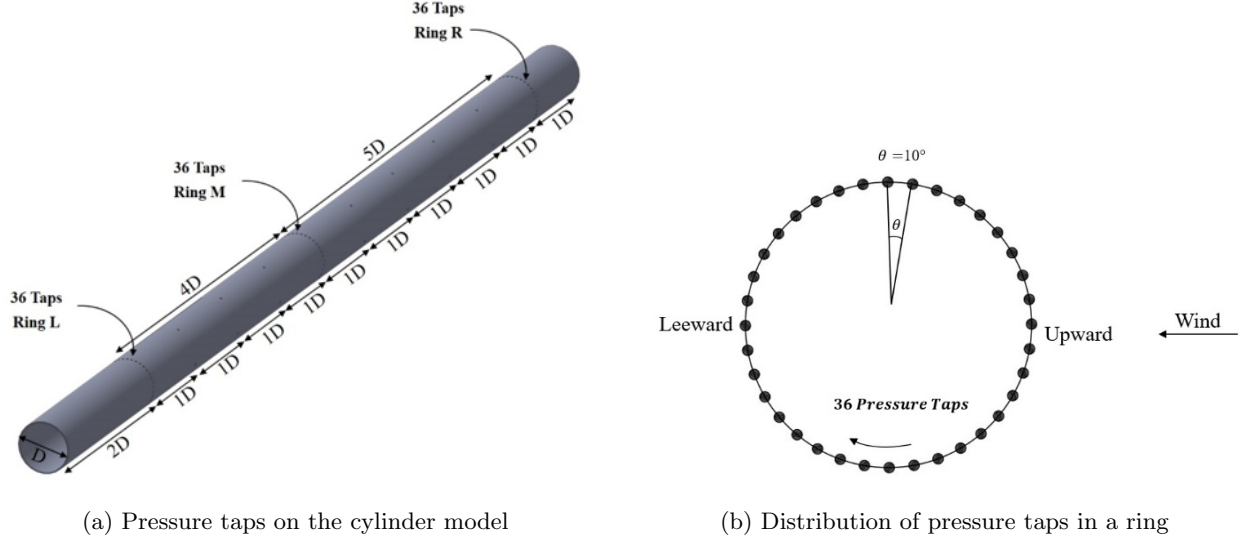
(a) Pressure taps on the cylinder model   (b) Distribution of pressure taps in a ring

Figure 3: Schematics illustrating the locations of surface pressure taps on the cylinder model.

4. Numerical Results and Verification with Measured Data

The objective of this paper is to demonstrate the capability of detached eddy simulations to predict aerodynamic loads on a static cylinder and an elastically-mounted cylinder. Verification with existing experimental data in the literature, and data from new experiments conducted as a part of this study, are presented for both the static cylinder and the elastically-mounted cylinder. Smooth inflow is used – zero turbulence in the numerical simulations and the minimum possible inflow turbulence intensity ($\sim$0.2%) in the tunnel. Cylinder surface is very smooth and hence surface roughness is not modeled in the simulations.

Static testing is performed for (1) flow normal to the cylinder axis, and (2) flow at an angle to the cylinder axis (inclined cylinder); three inclination angles are analyzed in this study. These cases are simulated at Reynolds number $Re_D = 20,000$ which is corresponding to laminar separation (LS), where flows are laminar before separation and transition to turbulence occurs in the shear layer.

Dynamic testing is performed for an elastically-mounted cylinder in eight different inflow reduce velocities with (1) flow normal to the cylinder axis, and (2) flow at an angle to the

cylinder axis (inclined cylinder). However, due to high computational cost of simulations, only one inclination angle is analyzed in the dynamic study(45°). The cylinder is limited to vibrate along the direction which is perpendicular to both the flow direction and the cylinder axis. All dynamic cases are simulated at the same Reynolds number, $Re_{D,n} = 20,000$.

4.1. Mesh Sensitivity Study

A mesh sensitivity study is performed for the normally-incident flow category for $Re_D = 20,000$. Table 1 presents a summary of the different cases simulated for this study. Three different meshes, labeled 'Mesh 1', 'Mesh 2', and 'Mesh 3' are shown in the table. The computational domain is $25 \times D$ in the radial direction and $10 \times D$ in the span direction.

Table 1: Summary of the test cases simulated to investigate sensitivity of results to mesh size

Re_D	Mesh name	Cell count(θ, r, z)
20,000	Mesh 1	157, 233, 65
20,000	Mesh 2	236, 343, 100
20,000	Mesh 3	354, 507, 150

Figure 4 compares the mean aerodynamic pressure coefficient, $\overline{C}_p = 2(\overline{p} - p_\infty)/(\rho V_\infty^2)$ obtained using simulations with different grids, and experimental data. Experiment I refers to data from Norberg (2013) and Exp-ISU is from our measurements. Simulations are simulated at 'cylinder diameter based' Reynolds number, $Re_D = 20,000$, which is the same as Experiment I, but the Re_D in Exp-ISU is higher ($Re_D = 51,500$) due to the limitation of the wind tunnel and measurement equipment.

Consistent with the results of Travin et al. (2000) and Breuer (2000), the simulation results are found to be sensitive to mesh size even with the highest mesh resolution attempted.

Mesh 2 and Mesh 3 capture the flow separation location correctly (same as in the experiment), but separation is delayed with Mesh 1. Results of Mesh 2 are in closer agreement with Experiment I, however they differ from the results of Mesh 3 in the separated flow region. Interestingly, the Exp-ISU data agrees well with Mesh 3 results in the same region. Based on this study, Mesh 2 is chosen for the subsequent simulations because it can predict aerodynamic loading and resolve wake turbulence reasonably accurately within a reasonable computational cost.
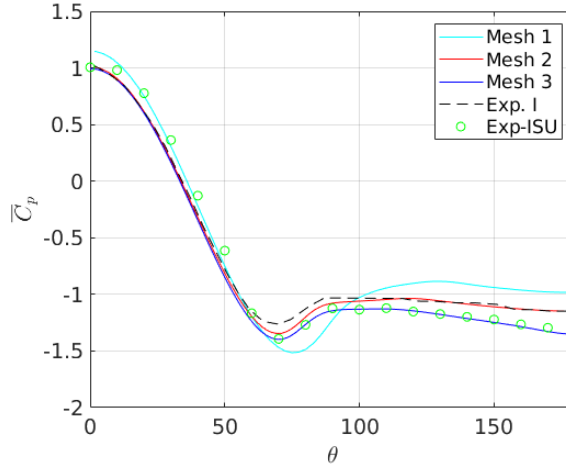
Figure 4: $\overline{C}_p$ comparisons between simulation results using different meshes.

4.2. Static Cylinder with Normally-Incident Flow

Table 2 summarizes the simulation results for the static case and compares them with two sets of experimental data. The peak shedding Strouhal number (St_p), the mean drag coefficient, $\overline{C}_d$ and the mean back pressure coefficient, $\overline{C}_{pb}$ are compared in the table. Strouhal number is a non-dimensional frequency, defined here as $St = f\,D/V_\infty$, and St_p corresponds to the peak vortex shedding frequency of the cylinder.

Figure 5 compares the predicted mean aerodynamic pressure coefficient, $\overline{C}_p$ and the root mean square of perturbation pressure coefficient, $C_{p'rms} = \left(\overline{C_p^2 - \overline{C}_p^2} \right)^{1/2}$ with the data from the two experiments. The predicted $\overline{C}_p$ agrees very well with the data from Experiment I;

Exp-ISU data shows slightly lower $\overline{C}_p$ than observed in Experiment I and the simulation, especially after 100°, and the mean back pressure, $\overline{C}_{pb}$ is lower as well. The prediction $C_{p'rms}$ distribution lies in between the two measurements. Both measurements as well as the simulation show the peak to be around 80°, which indicates the location of flow separation. The predicted distribution over the cylinder surface agrees well with the measurements.

Table 2: Summary of results for normally-incident flow simulations

Re_D	Method	St_p	$\overline{C}_d$	$\overline{C}_{pb}$
20,000	$k - \omega$ DDES	0.21	1.13	-1.16
20,000	Experiment I	0.19	1.22	-1.1
51,500	Exp-ISU	0.21	1.14	-1.3
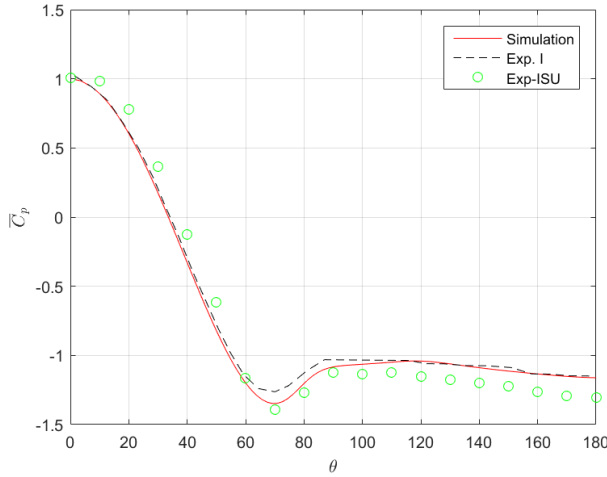
(a) Mean aerodynamic pressure coeff., $\overline{C}_p$
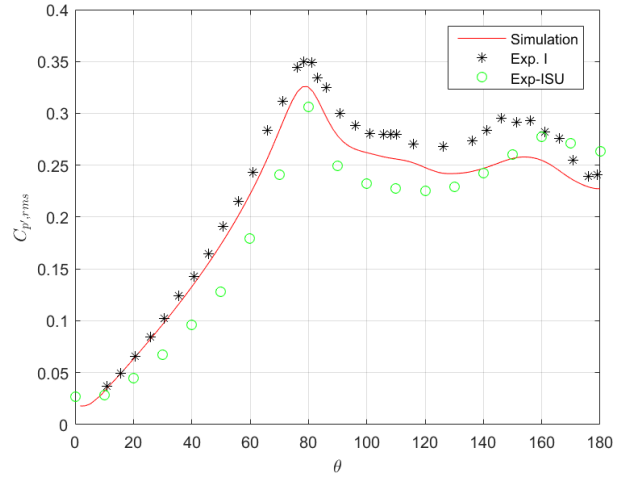
(b) r.m.s. of pressure coeff., $C_{p'rms}$

Figure 5: Comparisons of mean and rms of aerodynamic pressure coefficient between the simulation and experimental measurements.

Figure 6 plots the predicted and measured wake velocity profiles at the axial station, $x/D = 2$; the cylinder axis is located at $x/D = 0$. The peak wake deficit and the wake profile are predicted accurately. The measured data shows a slight asymmetry in the data,

14

which is perhaps due to asymmetry in the experimental setup (e.g., distance from the tunnel wall between the top and bottom surfaces of the cylinder). The simulation data is averaged over 120 wake shedding cycles and experimental data is averaged over 540 cycles.
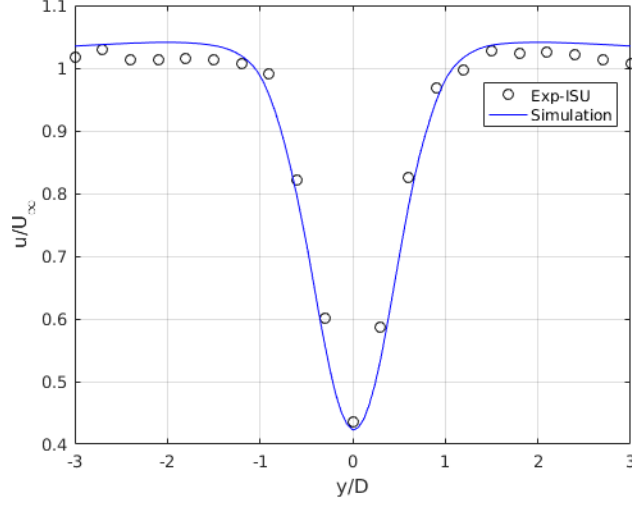

Figure 6: Comparison of predicted and measured velocity profiles in the cylinder wake $2D$ downstream of the cylinder axis.

Figure 7 presents predicted temporal variation of sectional lift and drag coefficients (C_l and C_d). As expected for a circular cylinder, the mean lift coefficient ($\overline{C}_l$) is zero but the mean drag coefficient ($\overline{C}_d$) is finite. The high-frequency oscillations, more apparent in C_l time history are due to Karman vortex shedding, which occurs at $St = fd/U \sim 0.2$ for bluff bodies in the range of Re_D considered here. In addition to the oscillations at the Karman vortex shedding frequency, the entire signal appears to modulate at a frequency which is an order of magnitude lower than that corresponding to $St = 0.2$. This modulation has a certain randomness to it and is not perfectly periodic. This modulation phenomenon has been reported elsewhere, see e.g., Travin et al. (2000).

Figure 8 (a) compares the power spectral densities of lift coefficient (C_l) between data from Exp-ISU and the simulation. The lift in the measurements is obtained by integrating the surface pressure measured using the pressure taps. Figure 8 (b) presents the DES computed
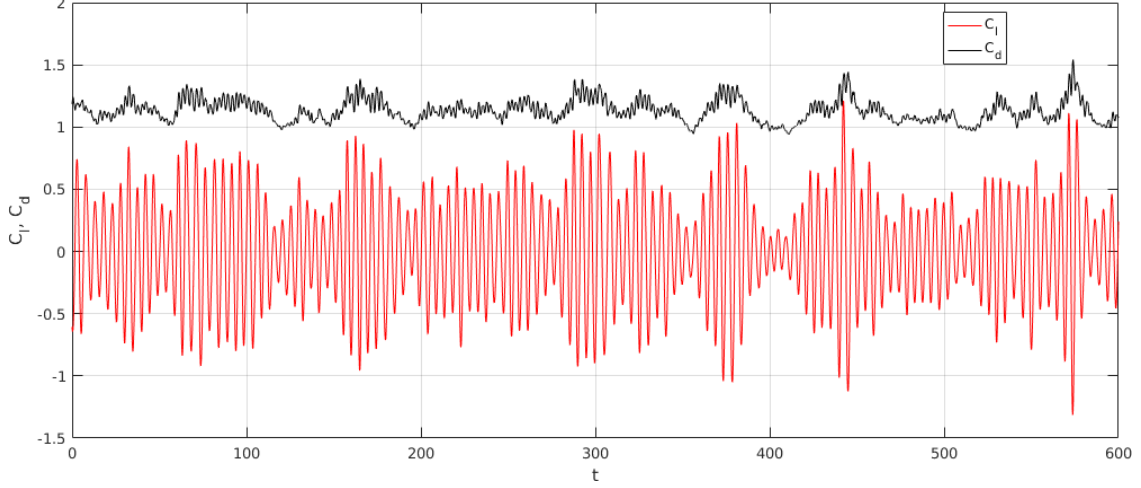
15

Figure 7: Predicted temporal variations of lift and drag coefficients

spectra of C_d. Because vortex shedding alternates between the top and bottom sides of the cylinder, one vortex shedding period contains two cycles of drag but only one cycle of lift. This can be seen in Figure 8, where the spectral peak for C_l occurs at f_p while the spectral peak for drag is at $2 \times f_p$, where f_p is determined by the peak shedding Strouhal number, $St_p = f_p D / V_\infty$. Based on existing literature (see Travin et al. (2000) and Norberg (2013)), $St_p \sim 0.2$. Both measurement and prediction agree very well with each other and show the peak for lift to be around f_p corresponding to St_p.

The peak frequency and its first three harmonics that occur at $St = 0.4, 0.6, \& 0.8$, are identified in the figure using vertical grid lines and labeled as $2f_p$, $3f_p$, $\& 4f_p$. The prediction and experiment both show a second, smaller peak in the lift spectrum at the third harmonic ($St = 0.6$). Since the lift vector alternates with the side the vortex sheds from, only odd harmonics of f_p (i.e., $3f_p$, $5f_p$, ...) are expected in the spectra. Therefore, no peak is observed in the lift spectra at the second harmonic ($St = 0.4$) or higher *even* harmonics in either the measured or the simulated data. The spectral shape of the PSD of C_l is correctly predicted, even though the magnitude is slightly higher than the measured data.
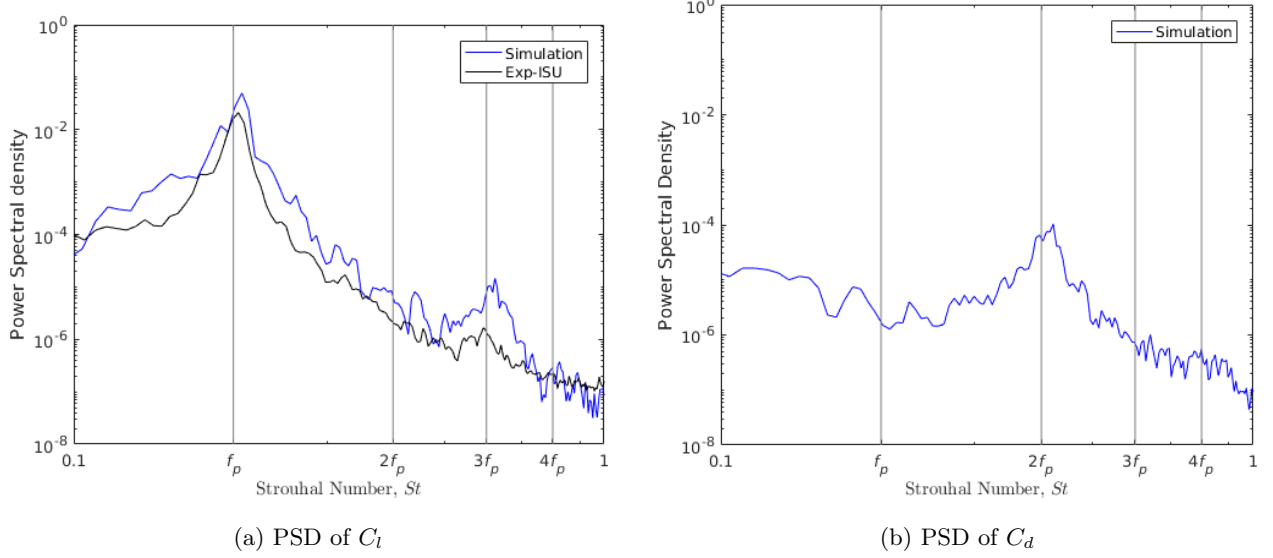
(a) PSD of C_l (b) PSD of C_d

Figure 8: Comparison of predicted and measured power spectral densities (PSDs) of C_l and C_d. The measured data here is from our experiments (Exp-ISU).

4.3. Static Cylinder with Yawed Flow (Inclined Cylinder)

Figure 9 is a schematic that illustrates the setup for the inclined-cylinder simulations. The relative inclination of the cylinder axis with respect to the flow is obtained by yawing the flow rather than inclining the cylinder; these simulations are therefore also referred to as yawed flow simulations. Other than yawing the inflow, the setup is exactly the same as for the normally-incident flow cases.

The yaw angle, β is defined as the angle between the inflow velocity vector $\boldsymbol{V_\infty}$ and the x axis; the cylinder is aligned with the z axis. The normal component of the flow velocity, V_n and the spanwise component, V_z are defined as $V_n = V_\infty \cos\beta$ and $V_z = V_\infty \sin\beta$, where $V_\infty = |\boldsymbol{V_\infty}|$. The computational domain is $10 \times D$ in the spanwise direction to resolve and investigate spanwise variation of aerodynamic forces. Three different yaw angles $\beta = 15, 30, \& 45$ degrees are investigated in these simulations.

Table 3 summarizes the peak Strouhal number (St_p) and the back pressure coefficient (C_{pb}) for four different flow yaw angles, $\beta = 0, 15, 30, \& 45$ degrees. The component of the
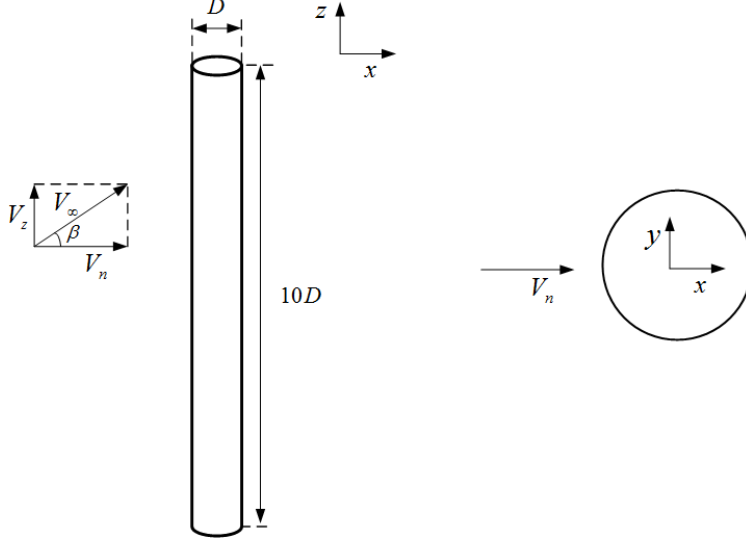
Figure 9: A schematic of the computational setup for static inclined cylinder simulations. The right figure is a cross-sectional view. The inflow is set to an angle with respect to the cylinder axis, which stays aligned with the z axis of the coordinate system.

freestream velocity normal to the cylinder axis is used as the reference velocity scale to define a new set of non-dimensional quantities, such as Reynolds number, $Re_{D,n} = \rho V_n D / \mu$, Strouhal number, $St_{p,n} = f D / V_n$, and aerodynamic pressure coefficient, $\overline{C}_{p,n} = 2(\overline{p} - p_\infty)/(\rho V_n^2)$. The peak shedding Strouhal number and the mean back pressure coefficient normalized in this manner are labeled respectively as $St_{p,n}$ and $\overline{C}_{pb,n}$. The measured value of $\overline{C}_{pb,n}$ is lower than predicted by the simulations (see Table 3), suggesting that the measured mean velocity at the back of the cylinder is slightly higher than predicted.

Figure 10 compares with measured data the predicted mean aerodynamic pressure coefficient $(\overline{C}_{p,n})$ and root mean square of perturbation pressure coefficient, $C_{p'rms,n}$ normalized using V_n, for $\beta = 30°$ case. The predicted distribution of $\overline{C}_{p,n}$ and mean back pressure, $\overline{C}_{pb,n}$ are found to be slightly higher than Exp-ISU data, which is consisted with the observation for the normally-incident flow cases. The predicted $C_{p'rms,n}$ distribution agrees very well with measurement, especially before 120°. The peak of $C_{p'rms,n}$ is observed around 80° in both experiment and simulation, which is indicative of the location of separation of the

Table 3: Summary of simulation results for four different flow yaw angles ($\beta = 0, 15, 30$, & 45 deg). Experimental data is only shown for $\beta = 30°$.

Method	flow angle, β	Re_D	$Re_{D,n}$	$St_{p,n}$	$\overline{C}_{pb,n}$
Simulation	0°	20,000	20,000	0.21	-1.15
Simulation	15°	20,000	19,318	0.21	-1.11
Simulation	30°	20,000	17,320	0.20	-1.11
Exp-ISU	30°	51,500	44,600	0.19	-1.27
Simulation	45°	20,000	14,142	0.21	-1.16

shear layer. Beyond $\theta = 120°$, the measured data shows higher $C_{p'rms,n}$ than predicted by the simulations. A similar underprediction is observed in the normally-incident flow case.
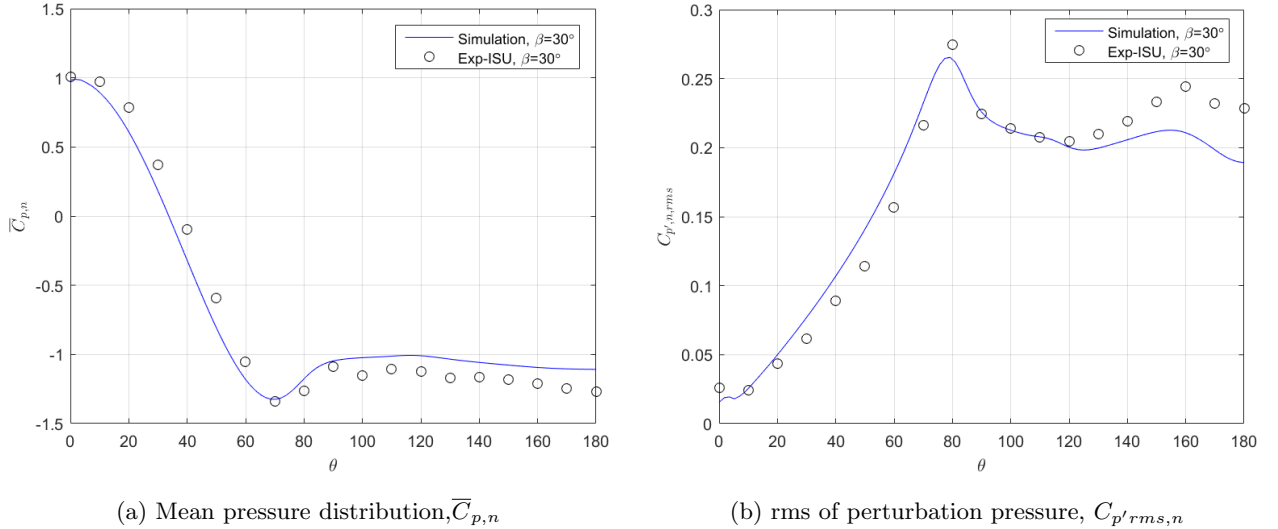

(a) Mean pressure distribution, $\overline{C}_{p,n}$

(b) rms of perturbation pressure, $C_{p'rms,n}$

Figure 10: Comparisons between simulation and experimental measurements for $\beta = 30°$ yawed-flow case.

Figure 11 presents predicted and measured wake velocity profiles for $\beta = 30°$ case at $x/D = 2$. The predicted peak wake deficit matches remarkably well with Exp-ISU data. However, the experimental data shows higher overshoots in streamwise velocity in the shear layer region than predicted by the simulations. The experimental data is also very slightly

19

asymmetric, which is likely due to the fact that the cylinder is located closer to one side of the tunnel wall. It should be noted that the asymmetry is very small and the wall effects are minimal.
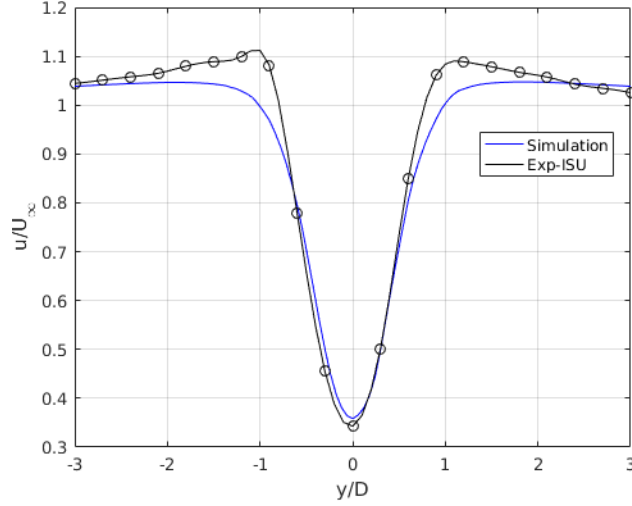

Figure 11: Comparison of predicted and measured velocity profiles for $\beta = 30°$ yawed flow in the cylinder wake $2D$ downstream of the cylinder axis

Figure 12 compares the power spectral densities of the transverse force coefficient (along the y axis), $C_{y,n}$ for $\beta = 30°$ case between Exp-ISU data and predictions, where $C_{y,n} = 2\,F_y/\left(\rho V_n^2(D \times L)\right)$, F_y is the net force over the entire cylinder; longitudinal force coefficient, $C_{x,n}$ is similarly defined. In the simulation, the first peak is observed around $St_{p,n} \sim 0.2$, which is the same as for the normally-incidence flow case (see Figure 8 (a)). The spectral shape is correctly predicted by the simulation although the measured curve appears to be shifted along the x axis; this is likely due to a scaling factor in frequency (log scale is used for frequency in Fig. 12), arising perhaps from a slight mismatch in the measurement of the inflow velocity in the experiment. Figure 13 compares the predicted mean aerodynamic pressure coefficient $(\overline{C}_{p,n})$ normalized using V_n, for four different values of inflow yaw angle, β. The distribution of $\overline{C}_{p,n}$ is found to be very similar irrespective of β; Zdravkovich (2003) refers to this as 'independence principle'. The independence principle is also observed in the
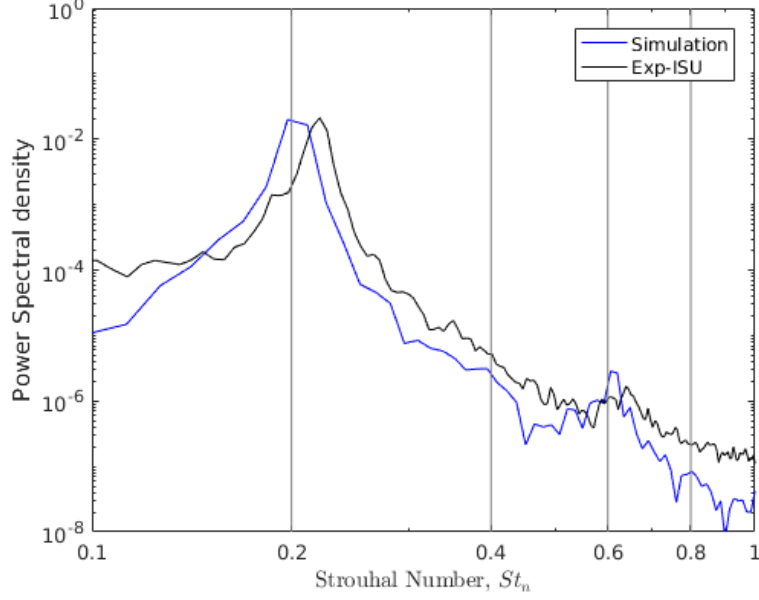
Figure 12: Comparison of predicted and experimental power spectral densities (PSDs) of force coefficient $C_{y,n}$ for $\beta = 30°$ yawed-flow cases.

power spectral densities of the transverse force coefficient, $C_{y,n}$ for the same set of values of β analyzed. Figure 13 (b) shows that the spectra collapse when V_n is used to normalize the force coefficients and the frequency; the abscissa in Fig. 13 (b) is St_n.

(a) Mean pressure coeff., $\overline{C}_{p,n}$
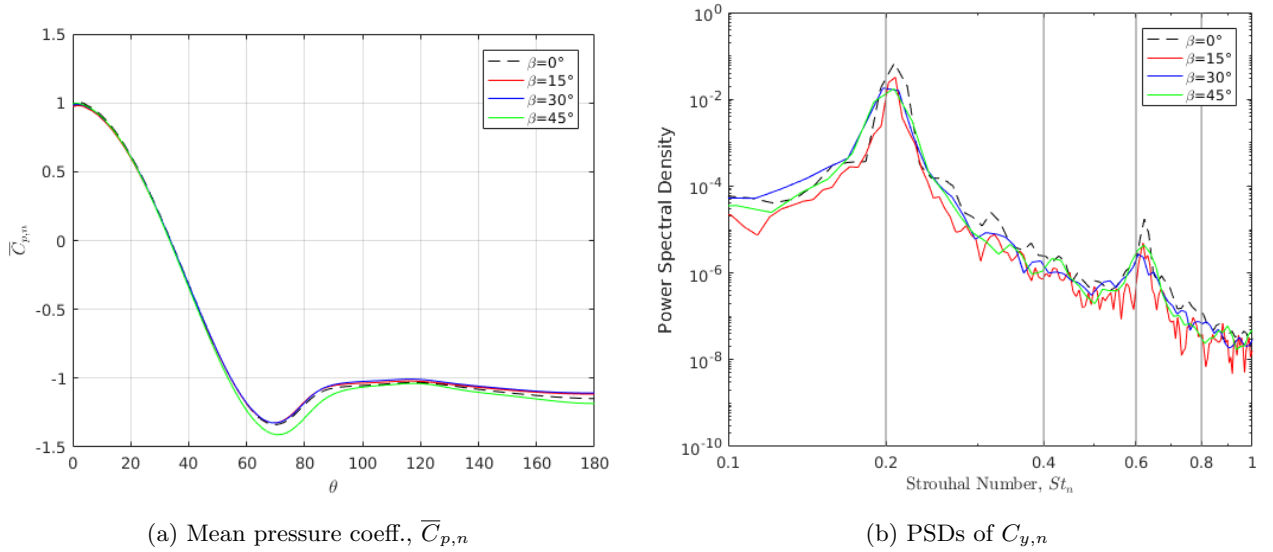

(b) PSDs of $C_{y,n}$

Figure 13: Independence principle: comparisons of (a) $\overline{C}_{p,n}$, and (b) power spectral densities (PSDs) of $C_{y,n}$ between predictions for various β values.

Figure 14 shows spatio-temporal plots of the the force coefficients $C_{x,n}$ and $C_{y,n}$. Here, $C_{x,n}$ and $C_{y,n}$ are functions of spanwise location and are computed by normalizing the sectional forces in x and y directions respectively ($C_{x,n} = 2\,f_x/(\rho V_n^2)$, where f_x is force per unit area in the x direction). The coefficients are plotted as functions of span (z) and time to obtain the contours shown in the figure. The contours clearly show that the force coefficients vary along the span, indicating that vortex shedding does not occur simultaneously along the entire span. In fact, a spatial drift from left to right with increasing time can be seen in the contours (more visible in the $C_{x,n}$ spatio-temporal plot) which is indicative of spanwise flow over the cylinder.
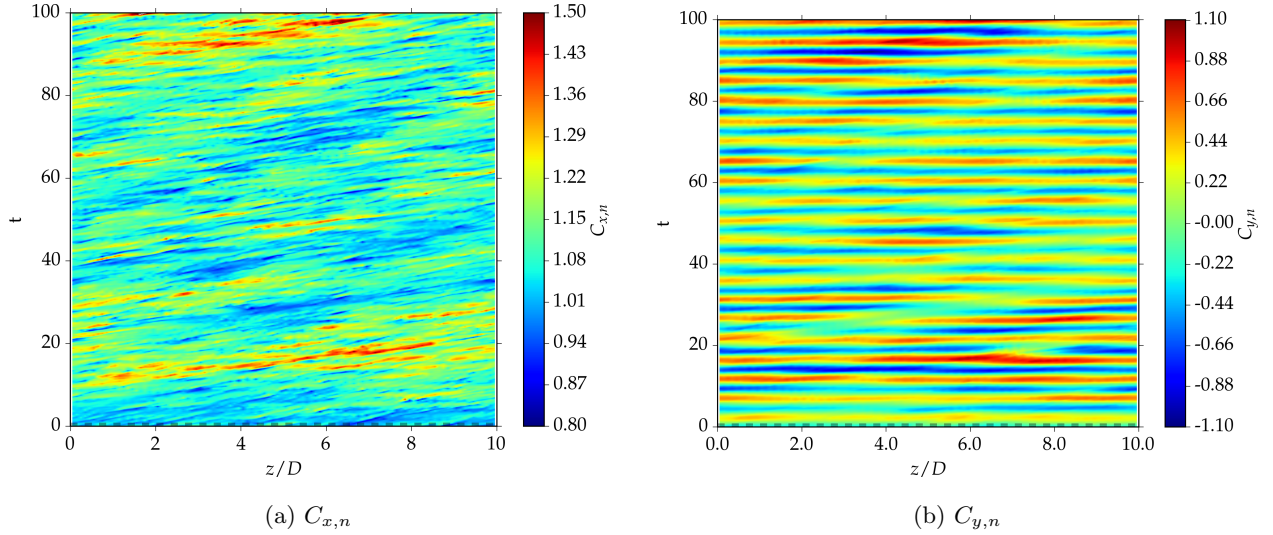

(a) $C_{x,n}$ (b) $C_{y,n}$

Figure 14: Spatio-temporal distribution of force coefficients at $\beta = 30°$

Figure 15 presents coherence of force coefficients for $\beta = 30°$ case. Magnitude squared coherence, $\gamma^2(\Delta z)$ is defined as

$$\gamma^2(\Delta z) = \frac{\langle |S_{xy}|^2 \rangle}{\langle S_{xx} \rangle \langle S_{yy} \rangle}, \tag{1}$$

where S_{xy} denotes cross-spectral density of the quantity ($C_{x,n}$ or $C_{y,n}$) at two points separated by a distance Δz, and S_{xx}, S_{yy} are auto-spectral densities; angular brackets denote ensemble averaging, however ergodicity assumption is used to relate that to time averaging. The

coherence plot of $C_{y,n}$ indicates that spanwise correlation is very high (over nearly the entire cylinder span) at the vortex shedding frequency, but is small at other frequencies, which is expected based on literature. $C_{x,n}$ however is not that highly correlated along the span even at the peak vortex shedding frequency.

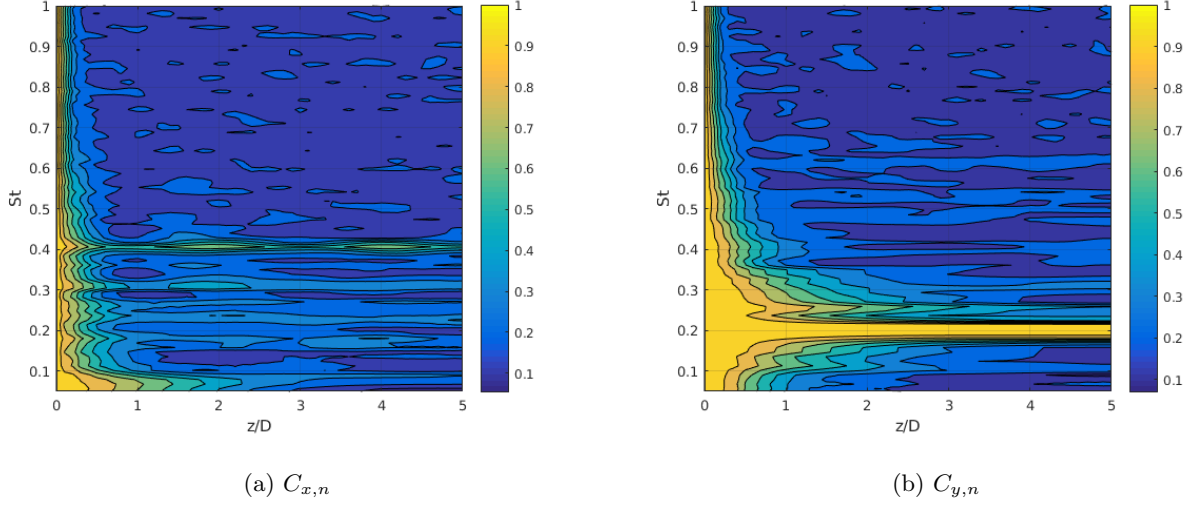(a) $C_{x,n}$ (b) $C_{y,n}$

Figure 15: Magnitude squared coherence, $\gamma^2(\Delta z)$ of transverse and longitudinal force coefficients, $C_{x,n}$ and $C_{y,n}$ for $\beta = 30°$ case.

4.4. Vortex-Induced Vibration (VIV)

A schematic of the setup for the vortex-induced vibration(VIV) simulations is presented in Figure 16. It is very similar for the static cylinder simulations, except for its additional mass-spring-damper system. In VIV simulations, mass ratio m^* is chosen as 2.6, where $m^* = m_s/(\rho\pi D^2/4)$, with m_s being the mass per unit length of the cylinder and ρ being the fluid density. The mechanical damping ratio of the system ζ is 0.001. The predicted results will be compared with Exp. II and Exp. III which refer to data from Franzini et al. (2013) and Khalak and Williamson (1997), respectively. The same mass ratio and damping ratio are chosen in simulations and Exp. II, while $m_s = 2.4$ and $\zeta = 0.0045$ are used in Exp. III. Because the simulations apply periodic boundary conditions at the span directions, the end effects are negligible for simulations, while they can not be neglect on both experiments.
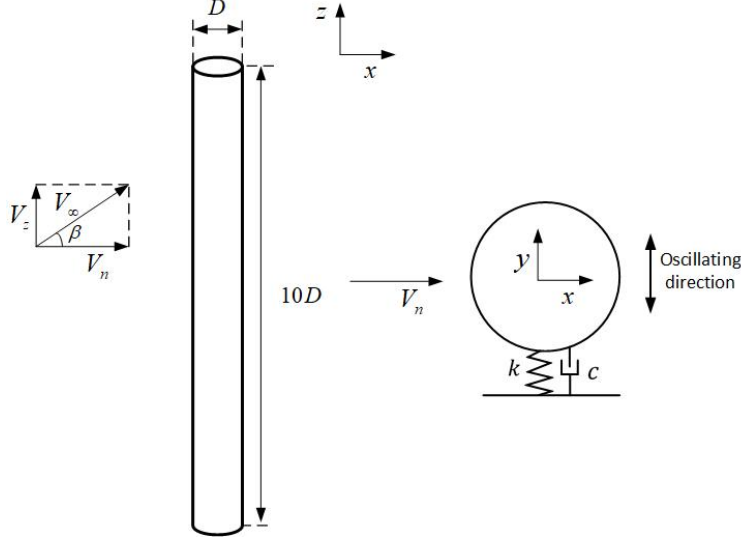
23

Figure 16: A schematic of the computational setup for oscillating cylinder simulations. The right figure is a cross-sectional view. The inflow is set to an angle with respect to the cylinder axis, which stays aligned with the z axis of the coordinate system.

Figure 17 compares predicted non-dimensional mean amplitude $\bar{A}/D$ with the experimental data for various reduced velocities $V_{R,n}$. The reduce velocity $V_{R,n}$ is defined as $V_{R,n} = V_n f_N / D$, with f_N being the natural frequency of the system. Two difference yawed angle inflows, $\beta = 0°$ and $45°$ with $Re_{D,n} = 20,000$ have been investigated in the simulation. Fig. 17 shows four distinct branches for Exp. III, namely the initial excitation branch, the upper branch, the lower branch and the desynchronization branch (Khalak and Williamson (1997)). In the initial excitation branch, the mean amplitude rapidly grows quickly as reduce velocity $V_{R,n}$ increases, which can be seen in simulations and both experiments. All simulations and experiments observe a peak in the upper branch. The predicted amplitude for $\beta = 0°$ case agrees very well with Exp. III, but is slightly smaller than Exp. II. Even though both yawed angle inflow simulations have a similar peak in the upper branch, the predicted non-dimensional mean amplitude $\bar{A}/D$ quickly drops to around 0.6 at $V_{R,n} = 5.9$ for $\beta = 45°$ case. Exp II presents very different results for $0°$ and $45°$ in the upper branch. Because the end effect plays an important role in the experiment, that might be the reason

to cause this difference. A lower branch region where the mean amplitude $\bar{A}/D$ is almost constant can be observed on simulations and Exp. III. Though similar lower branch is not being found on Exp. II, it is widely known and observed on other experiments by Govardhan and Williamson (2000). Overall, the predicted mean amplitude agrees very well with Exp. III, but presents some difference from Exp. II. Other than the upper branch, both yawed flow simulations have observed very similar amplitude for various reduced velocities.
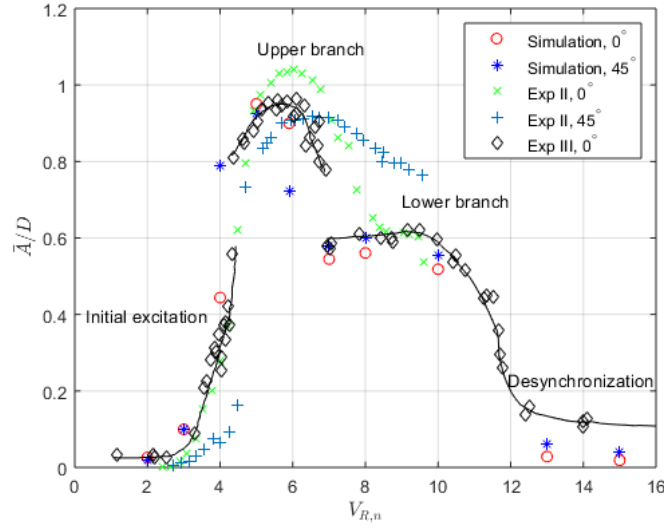

Figure 17: Comparison of predicted and experimental non-dimensional mean amplitude A/D for various reduced velocities $V_{R,n}$

Figure 18 presents non-dimensional frequency f/f_N for various reduced velocities $V_{R,n}$, with f being the vortex shedding frequency in the simulation while being the oscillating frequency in Exp. III because vortex shedding frequency data is not available in Exp. III. The blue dash line indicates vortex shedding frequency for the static cylinder ($St_p = 0.21$), while the red dash line presents the natural frequency. As the figure shown, the predicted non-dimensional frequencies for both yawed flows are very similar and agree very well with Exp. III. In the initial excitation branch, non-dimensional frequency f/f_N increases as reduced velocity $V_{R,n}$ increases, which follows the blue dash line. It suggests that the oscillating

motion is independent of the natural frequency of the system in the initial excitation branch. After that, the vortex shedding frequency locks onto the natural frequency f_N in the upper branch and lower branch, which is known as "lock-in". Because this is a low mass-damping system, the "lock-in" frequency is higher than the natural frequency, while it is significantly smaller than the vortex shedding frequency of the static cylinder. The similar phenomenon can also be observed on Exp. III. In the desynchronization branch, the vortex shedding frequency desynchronizes from the natural frequency indicating the ending of "lock-in".
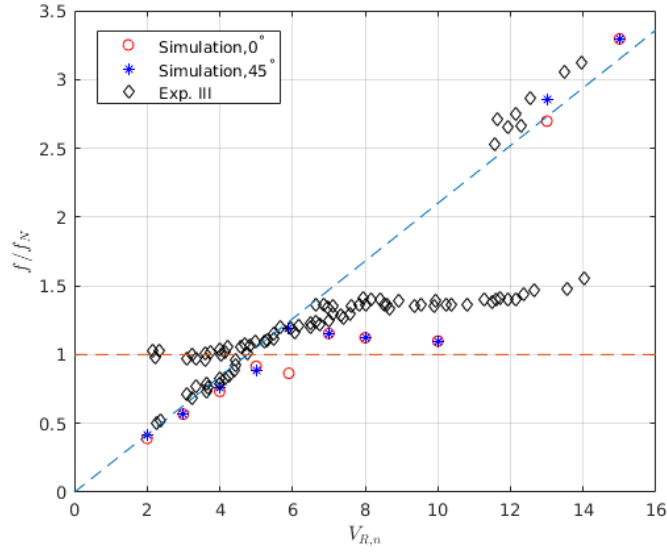

Figure 18: Non-dimensional frequency f/f_N for various reduced velocities $V_{R,n}$

As Fig. 17 shown, there is a jump between the upper branch and the initial excitation branch and another jump between the upper branch and the lower branch. This is because there are two different vortex shedding patterns happened in this reduced velocity region. Figure 19 displaces the Q-criterion for two reduced velocities $V_{R,n} = 4$ and $V_{R,n} = 8$ for $\beta = 45°$ case, which represent the typical vortex shedding modes of the initial excitation branch and the lower branch, respectively. As the figure shown, when $V_{R,n} = 4$, one vortex shedding period includes two singular vortexes (2S mode) shed alternately from either side of the cylinder. On the contrary, when $V_{R,n} = 8$ and "lock-in" happens, periodic vortex

shedding pattern switches to two pairs of vortexes (2P mode). Vortex shedding frequency lock onto the natural frequency as a result of 2P mode. The vortex shedding mode of the upper branch would shift between these two modes.
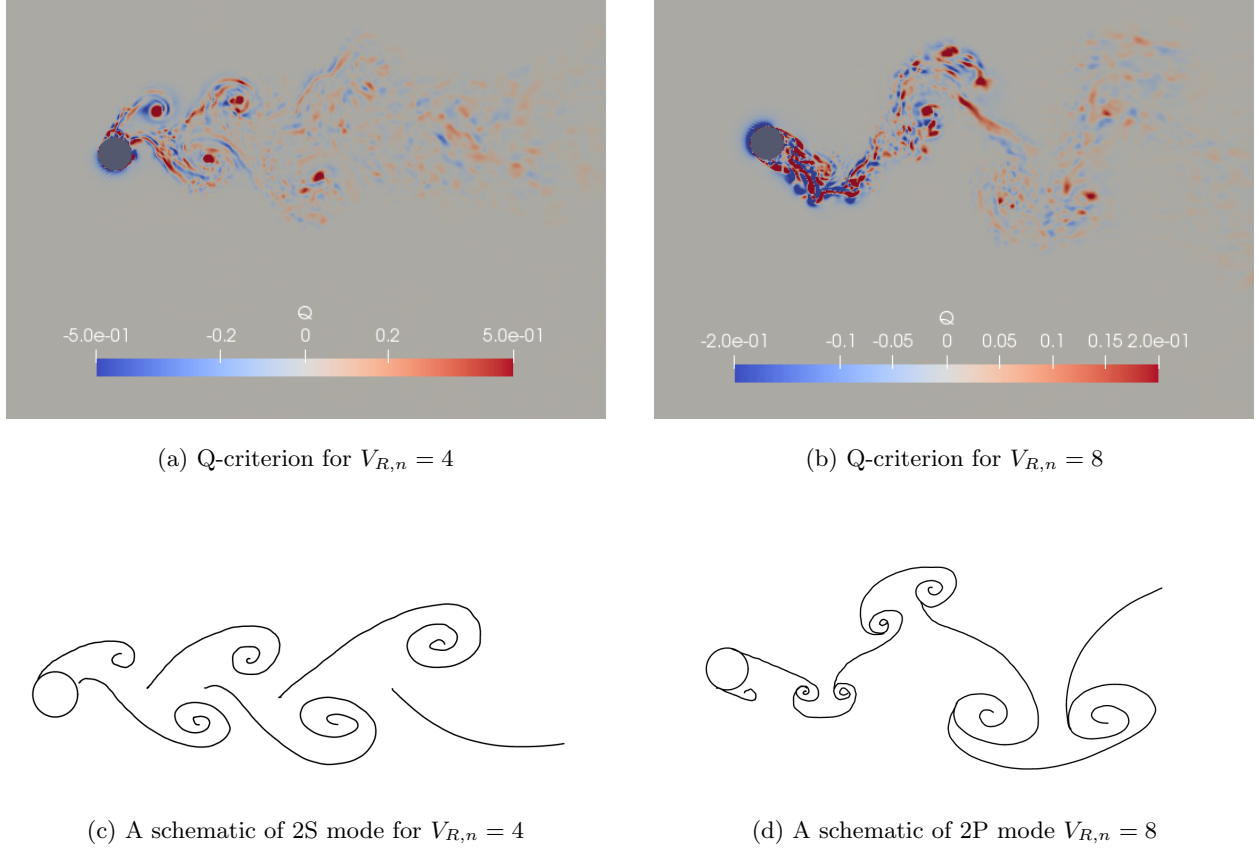

(a) Q-criterion for $V_{R,n} = 4$

(b) Q-criterion for $V_{R,n} = 8$

(c) A schematic of 2S mode for $V_{R,n} = 4$

(d) A schematic of 2P mode $V_{R,n} = 8$

Figure 19: Q-criterion and vortex shedding modes for $\beta = 45°$ yawed flow simulation

The force coefficients are shown in Fig. 20. It is well known that the vibration motion can significantly increase the fluctuation of forces. Mean transverse force coefficient $\bar{C}_{x,n}$ for reduce velocities $V_{R,N} < 5.9$ have a very similar curve as mean amplitude $\bar{A}/D$ in Fig. 17. However, mean amplitude $\bar{A}/D$ is almost constant in the lower branch while $\bar{C}_{x,n}$ continuously declines. The predicted rms of longitudinal force coefficients $C_{y,n,rms}$ has very sharp peak at $V_{R,n} = 4$, which is slightly different from Exp. II. Similar to $\bar{A}/D$ at $V_{R,n} = 4$, $C_{y,n,rms}$ for $\beta = 45°$ is much larger than $\beta = 0°$. Overall, two yawed angle flow simulations have very similar results for small amplitude vibrations. Independent principle can be

applied to forces coefficients except for the upper branch ($4 \leqslant V_{R,n} \leqslant 5.9$).
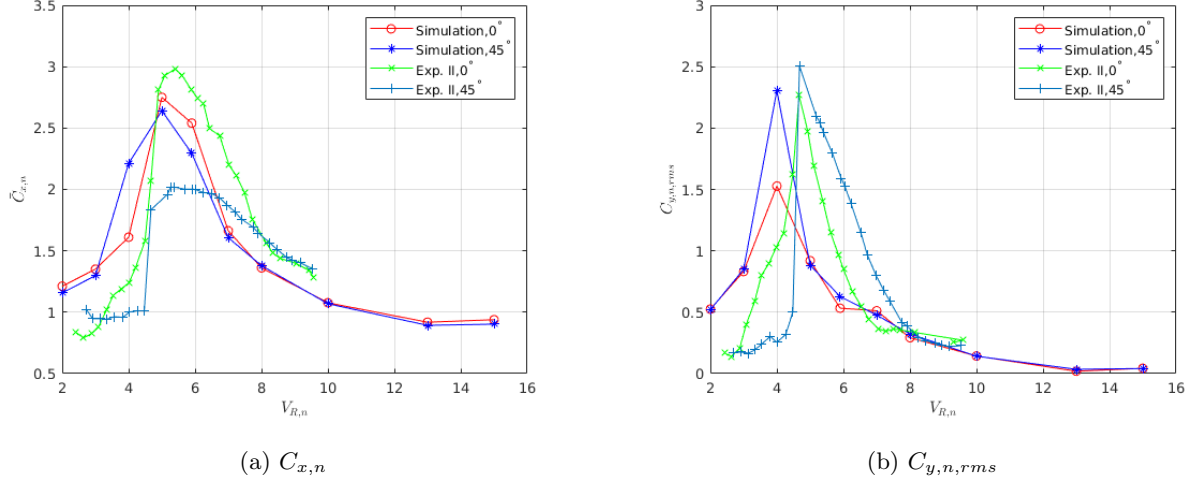

(a) $C_{x,n}$

(b) $C_{y,n,rms}$

Figure 20: Mean transverse and rms of longitudinal force coefficients, $\bar{C}_{x,n}$ and $C_{y,n,rms}$ for $\beta = 0°$ and $45°$ cases.

5. Conclusion

A computational methodology based on a $k-\omega$ delayed detached eddy simulation (DDES) model and in-house experiments are used to investigate aerodynamic loading on a smooth circular cylinder. Simulations are performed for the cylinder in normally-incident flow (static and dynamic) and yawed flow (3 cases). The computational methodology for predicting aerodynamic loading on the cylinder is verified against experimental data in normally-incident flow ($\beta = 0°$) and yawed flow ($\beta = 30°$). The agreement between the simulations and the experiments for normally-incident flow is very good, and the results of the yawed flow simulation with $\beta = 30°$ in reasonable agreement with the experiment. Overall, these comparisons show that the computational methodology is able to accurately predict aerodynamic loading on a static, smooth circular cylinder in smooth inflow.

Comparisons of simulation results for different flow angles (β) show that the aerodynamic loads do not vary with yaw angle when the loads and frequency are non-dimensionalized

using the component of the flow velocity normal to the cylinder axis. This indifference to yaw angle, referred to as the independence principle, is observed for yawed flow up to 45°.

The numerical study of VIV of an elastically-mounted cylinder in normally-incident flow agrees well with Exp III, but show some differences with Exp II. The difference might be caused by the end effects of the experiment. Other than the upper branch, the numerical results for two different yawed flow ($\beta = 0°$ and 45°) show reasonable agreement, which indicates independence principle is applicable for the most regime of VIV, except for the upper branch.

6. Acknowledgments

References

Bearman, P. W., 1984. Vortex shedding from oscillating bluff bodies. Annual review of fluid mechanics 16 (1), 195–222.

Breuer, M., 1998. Large eddy simulation of the subcritical flow past a circular cylinder: numerical and modeling aspects. International Journal for Numerical Methods in Fluids 28 (9), 1281–1302.

Breuer, M., 2000. A challenging test case for large eddy simulation: high reynolds number circular cylinder flow. International Journal of Heat and Fluid Flow 21 (5), 648–654.

Catalano, P., Wang, M., Iaccarino, G., Moin, P., 2003. Numerical simulation of the flow

around a circular cylinder at high reynolds numbers. International Journal of Heat and Fluid Flow 24 (4), 463–469.

Davenport, A., 1995. The dynamics of cables in wind. In: Proceedings of Symposium on Cable Dynamics.

Dong, S., Karniadakis, G. E., 2005. DNS of flow past a stationary and oscillating cylinder at. Journal of Fluids and Structures 20 (4), 519–531.

Feng, C., 1968. The measurement of vortex induced effects in flow past stationary and oscillating circular and d-section cylinders. Ph.D. thesis, University of British Columbia.

Franzini, G. R., Gonçalves, R. T., Meneghini, J. R., Fujarra, A. L. C., 2013. One and two degrees-of-freedom vortex-induced vibration experiments with yawed cylinders. Journal of fluids and structures 42, 401–420.

Govardhan, R., Williamson, C., 2000. Modes of vortex formation and frequency response of a freely vibrating cylinder. Journal of Fluid Mechanics 420, 85–130.

Jain, A., Modarres-Sadeghi, Y., 2013. Vortex-induced vibrations of a flexibly-mounted inclined cylinder. Journal of Fluids and Structures 43, 28–40.

Khalak, A., Williamson, C., 1997. Fluid forces and dynamics of a hydroelastic structure with very low mass and damping. Journal of Fluids and Structures 11 (8), 973–982.

Kravchenko, A. G., Moin, P., 2000. Numerical studies of flow over a circular cylinder at re d= 3900. Physics of fluids 12 (2), 403–417.

Norberg, C., 2013. Pressure forces on a circular cylinder in cross flow. In: IUTAM Symposium on Bluff Body Wakes, Dynamics and Instabilities, eds H Eckelmann, JMR Graham, P Hierre, PA Monkewitz. pp. 275–278.

Pontaza, J. P., Menon, R. G., Chen, H.-C., 2009. Three-dimensional numerical simulations of flows past smooth and rough/bare and helically straked circular cylinders allowed to undergo two degree-of-freedom motions. Journal of Offshore Mechanics and Arctic Engineering 131 (2), 021301.

Sarpkaya, T., 2004. A critical review of the intrinsic nature of vortex-induced vibrations. Journal of fluids and structures 19 (4), 389–447.

Spalart, P., Jou, W., Strelets, M., Allmaras, S., et al., 1997. Comments on the feasibility of LES for wings, and on a hybrid RANS/LES approach. Advances in DNS/LES 1, 4–8.

Travin, A., Shur, M., Strelets, M., Spalart, P., 2000. Detached-eddy simulations past a circular cylinder. Flow, Turbulence and Combustion 63 (1-4), 293–313.

Williamson, C., Govardhan, R., 2004. Vortex-induced vibrations. Annu. Rev. Fluid Mech. 36, 413–455.

Yeo, D., Jones, N., Meneveau, C., 2007. Characteristics of aerodynamic forces on a cylinder at different yaw and inclination angles under flow at high reynolds number. In: Proceedings of the 12th International Conference of Wind Engineering, Cairns, Australia. pp. 879–886.

Yeo, D., Jones, N. P., 2008. Investigation on 3-d characteristics of flow around a yawed and inclined circular cylinder. Journal of Wind Engineering and Industrial Aerodynamics 96 (10), 1947–1960.

Yeo, D., Jones, N. P., 2011. Computational study on aerodynamic mitigation of wind-induced, large-amplitude vibrations of stay cables with strakes. Journal of Wind Engineering and Industrial Aerodynamics 99 (4), 389–399.

Yeo, D., Jones, N. P., 2012. Aerodynamic forces induced by vertically oscillating incoming

flow on a yawed horizontal circular cylinder. Journal of Wind Engineering and Industrial Aerodynamics 104, 188–195.

Yin, Z., Reddy, K., Durbin, P. A., 2015. On the dynamic computation of the model constant in delayed detached eddy simulation. Physics of Fluids 27 (2), 025105.

Zdravkovich, M. M., 2003. Flow around Circular Cylinders: Volume 2: Applications. Vol. 2. Oxford university press.

Zhao, M., 2015. The validity of the independence principle applied to the vortex-induced vibration of an inclined cylinder in steady flow. Applied Ocean Research 53, 155–160.

Zhao, M., Cheng, L., Zhou, T., 2009. Direct numerical simulation of three-dimensional flow past a yawed circular cylinder of infinite length. Journal of Fluids and Structures 25 (5), 831–847.